Organic Electronics 13 (2012) 66–70

Contents lists available at SciVerse ScienceDirect

Organic Electronics

journal homepage: www.elsevier.com/locate/orgel

Electric field and charge distribution imaging with sub-micron resolution in an organic Thin-Film Transistor

Calogero Sciascia [a,*], Michele Celebrano [b], Maddalena Binda [a], Dario Natali [a,c], Guglielmo Lanzani [a], Juan R. Cabanillas-Gonzalez [d]

[a] CNST IIT@Politecnico di Milano, via Pascoli 70/3, 20133 Milano, Italy
[b] Physics Department, Politecnico di Milano, Piazza Leonardo da Vinci 32, 20133 Milano, Italy
[c] Electronics Department, Politecnico di Milano, Piazza Leonardo da Vinci 32, 20133 Milano, Italy
[d] Madrid Institute for Advanced Studies (IMDEA) in Nanoscience, Facultad de Ciencias, Av. Tomas y Valiente 7, Cantoblanco, 28049 Madrid, Spain

ARTICLE INFO

Article history:
Received 21 July 2011
Accepted 23 September 2011
Available online 20 October 2011

Keywords:
Electro-Reflectance
Stark shift spectroscopy
Confocal microscopy
Copper-Fluorinated Phthalocyanine
Mapping
Thin-Film Transistor

ABSTRACT

Here we show how Stark spectroscopy, coupled with confocal microscopy, is able to directly map the electric field in an n-type Copper-Fluorinated Phthalocyanine Thin-Film Transistor (TFT) under different operating conditions. To this extent, we locally probe Electro-Reflectance, with a nominal spatial resolution better than 500 nm, exploiting the fact that the detected signal is directly proportional to the square of the local field on the probe volume. This electric field imaging technique has unique advantages because it is non-invasive, since it exploits low incident power and because it probes the existing field in the bulk rather than the surface. Combining the experimental data with numerical modeling, it is possible not only to reconstruct the space charge profile in the few-nanometer thick accumulation layer, but also to extract the AC electron mobility.

1. Introduction

Many applications envisioned in organic electronics, like sensoristics, displays, smart packaging, etc. [1], require the development of performing Thin-Film Transistors (TFTs). However, the optimization of performances required for such applications demands a deep understanding of the device physics that we are still lacking in many cases.

While for inorganic semiconductors the equations describing charge injection and transport are completely set [2], the same does not hold true for carbon-based materials [3–6]. Intrinsic complexity of disordered organic systems makes them not theoretically accessible as their crystalline counterparts. In fact, organic semiconductors are chemically and morphologically inhomogeneous causing fluctuations at the microscopic level in both average and variance of electronic levels distribution [7]. As far as the charge transport, no consensus exists on how to model its dependence on charge density, electric field and disorder [6,8–11]. Nor is the interpretation of charge injection straightforward. In most cases, metallic–organic interface cannot be simply described in term of Mott-Schottky barrier because interface dipoles, still not easy to be predicted, arise in consequence of pillow effect, Fermi level pinning, chemical reactions, etc. [12,13].

The relatively poor knowledge and engineering of metal–organic interfaces often results in oTFTs suffering of contact resistances that in addition can show a non-linear dependence from applied electric field [14].

In this framework it appears evident the importance of a tool for detecting the electric field in the channel of a working device. The major techniques used for electric field detection in organic electronics are Electrical Force Microscopy (EFM) and Kelvin Probe Microscopy (KPM).

* Corresponding author. Tel.: +39 02 23999896; fax: +39 02 23996126.
E-mail addresses: calogero.sciascia@iit.it (C. Sciascia), michele.celebrano@polimi.it (M. Celebrano), maddalena.binda@iit.it (M. Binda), dario.natali@polimi.it (D. Natali), guglielmo.lanzani@iit.it (G. Lanzani), juan.cabanillas@imdea.org (J.R. Cabanillas-Gonzalez).

1566-1199/$ - see front matter © 2011 Elsevier B.V. All rights reserved.
doi:10.1016/j.orgel.2011.09.023

The KPM (EFM) methods are sensitive to the electric potential (or its gradient) at the probe. The remote field sensing of the AFM-based methods may lead to problems in resolution and interpretation of the signals [15]. In particular, in bottom-gate oTFT the most intriguing physics plays at the buried interface between the semiconductor and the gate insulator where solid probes cannot usually penetrate. The AFM methods may detect buried charges but such vertical sensitivity is paid in terms of lateral resolution. Optical methods such as confocal microscopy are instead sensitive to the electrical field in the volume of the optical beam which has a typical spatial lateral resolution of $\lambda/2{\cdot}NA$, with λ the light wavelength and NA the numerical aperture of the optical objective [16]. This leads to considerable advantages in terms of localization and interpretation of the signal. Being techniques of not invasive nature they do not modify the system of study or its boundary conditions. Moreover high operation bandwidths can be easily implemented which enables for instance fast data acquisition [17–19].

In the present work, we map the electric field distribution of the active area of an oTFT in operating conditions with an all-optical technique which overcomes some of the previous limitations. The basic idea consists of measuring the Electro-Reflectance (ER) response coming from the organic layer – proportional to the square of the electric field module – taking advantage of submicron spatial resolution of a confocal microscope [19]. For this purpose we use a non-perturbative optical field, with considerably low incident laser intensity (average power <100 nW) and a reduced risk of optical damaging. In fact, all our measurements were performed in ambient conditions and we do appreciate good signal stability over hours of continuous irradiation. The good lateral resolution (better than 500 nm) combined with sensitivity at bulk level allows us to monitor electric field profile coming from few-nanometers thick accumulation layer. The paper is organized as follows: in Section 2 the experimental set-up is outlined; in Section 3 the Electro-Reflectance data are presented; in Section 4 measurements and simulations are combined to extract electrical field and charge profile and finally the conclusions are given.

2. Materials and methods

The far field ER measurements are performed in a standard set-up using a halogen lamp (ASB-W-30, Spectral Products), filtered from single monochromator (CM 112, Spectral Products with 0.3 mm slits) and detected through a Si photodiode (SM1PD1A, Thorlabs). The signal is then processed with a lock-in amplifier from Stanford Instruments. The electrical sources are an amplified Hewlett–Packard function generator (mod. 3310A) and a power supply (E3648A from Agilent). For the microscopic ER set-up, the photo-detector and the acquisition system is the same as the far field system, but the probing light is provided by a Ti:Sapphire tunable laser with power below 100 nW to minimize photo-degradation of the organic film. The focusing apparatus is composed by a confocal microscope (with 0.75-NA long-working distance objective) in reflection configuration. Images are obtained by raster-scanning the sample with respect to the beam through a 3D piezo stage (P-517, Physik Instrumente) in the (x, y) plane, with the z axis used for focus fine optimization. As far as oTFT, the gate electrode consists of highly doped silicon underneath a 130 nm silicon dioxide layer, which acts as insulator. On top of silicon dioxide, a set of interdigitated gold electrodes (with chromium adhesion layer) are deposited by photolithographic technique. For our measurements, we used devices with channel length of 12 μm with a typical gold thickness of 100 nm. As final step, we evaporate a 40 nm thick film of $CuPcF_{16}$ at maximum pressure of 10^{-5} mBar and with deposition rate of 0.2 nm per second. The final thickness of organic layer is kept smaller compared with electrodes in order to avoid interferometer artefacts on top of the electrodes, known as *dark electrode effect* [20], as well as to avoid *charge broadening* over the metallic fingers [21]. The material is provided by Sigma–Aldrich and we did not perform any further purification or target surface functionalization. The device behaves as an electron only transporter, with charge mobility μ_e, evaluated from trans-characteristic curve [22], around 5×10^{-7} cm^2/Vs in air and 10^{-5} cm^2/Vs in vacuum. In spite of this modest mobility (likely attributed to the purity degree of the material and to the absence of functional groups on the oxide surface) [23], this material is suitable for ER confocal experiments owing to its high photochemical stability in air as well as large ER response at the 780 nm, tuned to the fundamental wavelength of the Titanium:Sapphire laser [24,25]. Simulations were performed using PDETOOL in MATLAB 7.4.0 environment.

3. Results

As starting point for the microscopic analysis we measured the ER response from the interdigitated array area taken with a standard "macroscopic" set-up. ER is a well-established technique measuring reflectance variation as function of an applied voltage. In order to remove artefacts due to fluctuations in optical density, spectra are normalized to the zero field reflectance as $(R^{on}-R^{off})/R^{off}$, where the apexes *on* and *off* stay for the presence and absence of applied field and R for reflectance. ER is widely used in solid state physics, and both the intensity and spectral shape of the signal are ruled by the external electric field $\vec{F}$ [26,27].

According to perturbation theory, the electric field leads both to an energetic shift of the electronic levels (ΔE) and to a re-distribution of the oscillator strength among different states (Stark shift). Such variations affect the dielectric constant and in ultimate analysis the reflectance.

In case of an isotropic distribution of molecules:

$$\Delta R \propto \frac{\partial \alpha}{\partial E}\frac{1}{2}\vec{F}\Delta\overleftrightarrow{p}\vec{F} + \frac{1}{6}\frac{\partial^2\alpha}{\partial E^2}(\Delta\vec{m}\vec{F})^2 \propto \left\|\vec{F}\right\|^2 \quad (1)$$

with α the absorption coefficient, $\vec{m}$ the permanent dipole of the molecule and $\overleftrightarrow{p}$ the polarizability tensor. In addition to Stark shift, usually dominant in organic molecules, optically-active field-induced species, such as polarons and bipolarons can also affect and play a role in determining the

ER signal [28]. To confirm that reflectance modulation arises exclusively from Stark shift and to rule out spectroscopic features of charged species, we repeated the experiment under different oTFT bias conditions. We compared spectra acquired when carriers accumulation occurred (obtained modulating the gate to source voltage and keeping the drain grounded), to spectra acquired without carriers accumulation (obtained modulating the drain to source voltage while keeping the gate grounded). Fig. 1 shows that the same spectral features over the 600–900 nm spectral range are obtained, thus proving the Stark-effect origin of the signal.

Furthermore the out-of-phase component (not reported here), related to the presence of long-living species, is zero for frequencies up to 3 kHz. Since polaron absorption is often delayed with respect to the field phase due to the interplay of charge trapping – recombination kinetics, this supports a negligible role of charge induced absorption in defining the ER. Moreover the results are in agreement with spectroscopic studies performed on related phthalocyanines [29].

Fig. 2 reports the profile of confocal R and ER profiles at 780 nm along two channels within the interdigitated area when $V_{DS} = 0$ V and $V_{GS} = 15\,V(1 + \sin(2\pi ft))$, being the frequency f set at 1 kHz. The R profile depends on the geometry and the materials composing the oTFT rather than its electrical polarization. It highlights the topography of electrodes, appearing as well-defined bumps emerging from a flat background due to the difference in reflectance between gold and silicon dioxide. From the analysis of the leading edges, it is possible to infer an optical lateral resolution better than 500 nm.

The effect of the drain voltage modulation on the ER distribution is displayed in Fig. 3. The 1D scans represent ER distribution under $V_{DS} = 15\,V(1 + \sin(2\pi ft))$ when V_{GS} is 22 and 0 V (panel A and B respectively). In both cases the ER profile is higher close to the drain side, the peak being more shallow when $V_{GS} = 22$ V, and more sharp and intense when $V_{GS} = 0$ V.

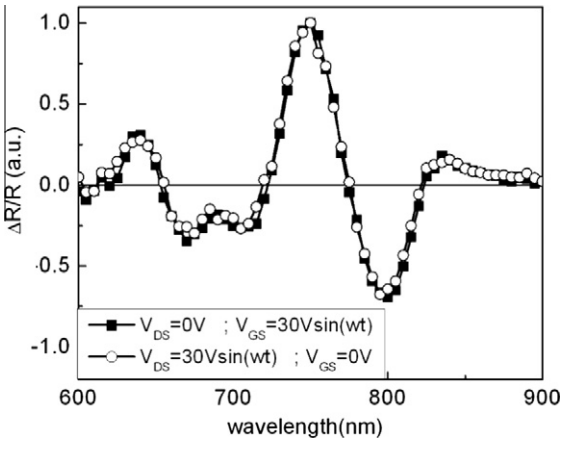

Fig. 1. Normalized ER spectra measured modulating the Gate (black filled squares) or the Drain (white open circles) with respectively Drain and Gate at 0 V. Considering that charge injection is expected to occur in the former case only, the fact two spectra have identical shape rules out polaronic features in this wavelength range. Hence the signal is purely due to Stark shift.

4. Discussion

First, we discuss scans with $V_{DS} = 0$ V and $V_{GS} = 15\,V(1 + \sin(2\pi ft))$, reported in Fig. 2. This electrical situation corresponds to the simplest one, where no significant net current is expected to flow since the source and drain are at the same potential, while a large density of charge is expected to be accumulated at the oxide/semiconductor interface due to V_{GS}. The obtained ER profile displays two symmetric sharp peaks, close to drain and source electrodes, gradually decreasing towards the center of the channel and abruptly vanishing in correspondence of electrodes. The symmetry is a consequence of source and drain equipotentiality, while the absence of ER on electrodes comes from the electric shielding from underneath metal. From a qualitative point of view, the constant (DC) bias $V_{GS} = 15$ V induces a spatially uniform accumulation layer within the organic film. The alternate (AC) voltage $V_{GS} = 15\,V\sin(2\pi ft)$ injects and sweeps away carriers every $1/f$ period. Efficient electron drift would lead to fast carrier re-distribution giving a spatially uniform time-dependent charge sheet. On the contrary if the mobility of electrons is modest, as in our case, short penetration from source and drain into the channel is expected even at moderate modulation frequency. The result is a space-dependent charge density, which in turn is responsible for the measured non-constant ER profile.

We now turn to a quantitative analysis, and we compare measured ER data with numerical solution of Laplace equation with static field in order to extract the charge distribution. It is to be stressed that the numerical model being purely electrostatic, it does not postulate any mechanism about charge injection or transport, and consequently the nature of these two phenomena does not influence the accuracy of the simulation. According to the geometrical symmetry, we set our differential problem in a two dimensional frame corresponding to a transverse section of the device (the longitudinal dimension can be rigorously neglected because there is no voltage gradient along electrodes). In order to determine the space charge distribution we use an optimization iterative procedure described hereafter. It is to be noted that, at the reference frequency f, since the Stark shift is proportional to the square of the field, the *ER* signal is given by the product between the DC and the AC electrical field amplitude [30]. As to the DC term, it can be readily computed imposing a constant charge density that completely shields the electric field from the gate under Dirichlet boundary conditions $V_{GS} = 15$ V and $V_{DS} = 0$ V. As to the AC term, we set the AC injected charge as the *unknown variable* to be adjusted in order to minimize the square of the difference between simulated ($\sim \boldsymbol{F}_{DC} \cdot \boldsymbol{F}_{AC}$) and experimental ER data.

Fig. 4A reports the simulated ER compared with the measured one. Panel B reports the corresponding calculated charge density profile, shown as sum of DC and AC terms. As expected, the maxima and minima are located close to the electrodes, where the injection occurs, and

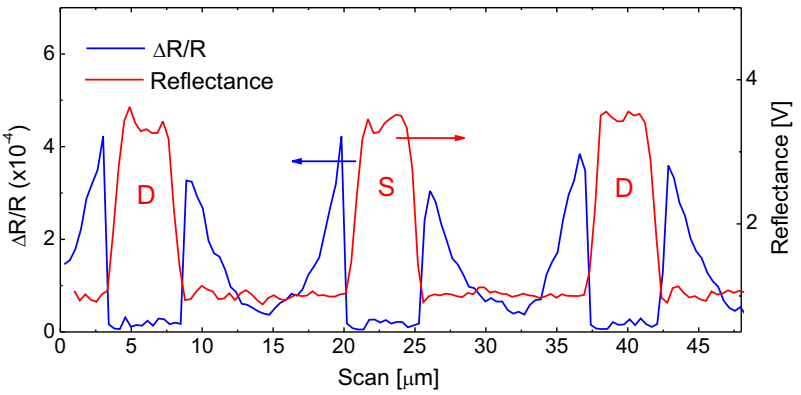

Fig. 2. The red line corresponds to Reflectance (R) profile, the blue line is the Electro-Reflectance (ER) profile when a modulated gate voltage is applied; V_{GS} = 15 V(1 + sin($2\pi ft$)) and V_{DS} = 0 V. ER signal is proportional to the squared module of the local electric field. R is expressed as the voltage read out by the photo-detector during the scan, while ER is the ratio between ΔR and R, with ΔR is the variation of Reflectance induced by the modulated applied voltage. R signal resembles the electrodes topology and gives indication about the lateral spatial resolution of the system (~500 nm). The probing light for both R and ΔR is the emission from a mode-locked Titanium:Sapphire laser tuned at 780 nm. (For interpretation of the references to colour in this figure legend, the reader is referred to the web version of this article.)

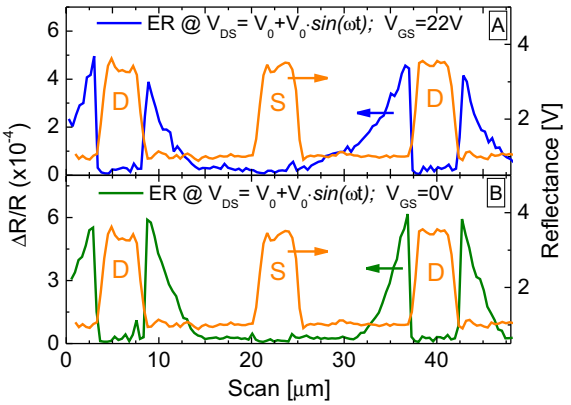

Fig. 3. ER maps of the transistor when an alternated voltage is applied between drain and source and: (A) applied Gate bias V_{GS} is 22 V or (B) V_{GS} is constantly kept at 0 V. Letters S and D locate respectively the position of the source and the drain electrodes. We observe a reversible and reproducible ER dwindling and flattening when the Gate voltage is applied.

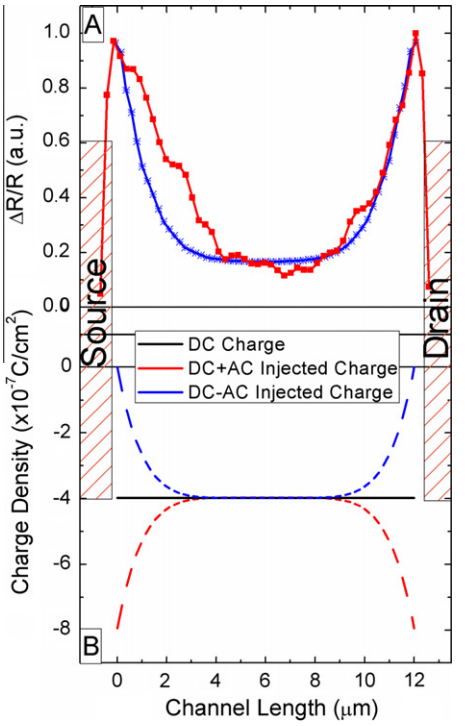

Fig. 4. (A) Measured (red squares) and simulated (blue stars) ER signal at V_{DS} = 0 V and V_{GS} = 15 + 15 V·sin($2\pi ft$). (B) The black solid line is the steady state charge induced by DC V_{GS} bias, red and blue dashed lines are the charge densities due to the AC V_{GS} component. (For interpretation of the references to colour in this figure legend, the reader is referred to the web version of this article.)

the profile flattens toward the middle of the channel (Fig. 4B), where it attains the value of a capacitor with voltage difference (DC) V_{GS} = 15 V and specific capacitance $\varepsilon_r \cdot \varepsilon_o / t$ (ε_o the vacuum permittivity, ε_r the relative permittivity and t the thickness of SiO_2 layer). The electron penetration depth from the contacts into the channel is about 2 μm upon the 1 kHz modulation. Combining this information with the longitudinal electric field (~60 kV/cm) resulting from the calculated charge profile, we can estimate the carrier mobility μ_e ($\mu_e = 2 \cdot d / F \cdot \tau$, being d the electron penetration depth, F the magnitude of the longitudinal electric field and τ the period of the modulation). Interestingly enough, the mobility turns out to be 0.6×10^{-5} cm^2/Vs, thus more similar to the value obtained *in vacuum* from transfer characteristic curves, than to value obtained in ambient atmosphere from analogous measurements (remind that ER measurements were performed in ambient atmosphere). This can be explained considering that ER measurements give access to the AC mobility, filtering out processes with characteristic long relaxation times. Thus if the modulation frequency is high enough, it can bypass deep traps often associated to the presence of oxygen or moisture. In addition, we can also deduce that trapping/

detrapping occurs in air on a time scale larger than the modulation period (few hundreds of microseconds) [31].

This electro-optical technique for the measurements of the AC mobility in oTFT, which basically relies on the choice of a modulation period shorter that the carrier transit time, is advantageous with respect to all-electrical techniques since it avoids the non-trivial management of stray and device capacitances [32].

We now turn to drain–source modulation $V_{DS} = 15\ V(1 + \sin(2\pi ft))$ and DC gate voltage $V_{GS} = 22$ V, shown in Fig. 3A. From a qualitative point of view, the DC terms of V_{GS} and V_{DS} induce a non-uniform accumulation layer that is periodically shaped by the AC drain–source component. Similarly to the case under zero drain–source field, modest electron mobility will likely limit carrier re-distribution. The region of the channel close to the drain actually contains information about the mobile charge injection/extraction, while the region close to the source is almost insensitive to this process (as the gate to source voltage is fixed). The influence of carrier accumulation on ER profile can be visualized when comparing Fig. 3A and B. Fig. 3B depicts the case where drain–source bias is modulated whereas the gate is grounded, i.e. negligible injection. Under these conditions the ER profile reflects a sharp peak close to the drain due to the so-called *blade effect* which intensifies the electric field in proximity of sharp geometry, i.e. electrode edge [33,34]. Compared to Fig. 3A, the absence of accumulation layer in Fig. 3B is reflected on a sharper ER profile solely dependent on the boundary conditions. In this case electrostatic shielding from accumulation layer is absent and all field lines end into drain edge.

5. Conclusion

We image with sub-micron resolution the electric field across the channel of an oTFT. The Stark signal coming from probe areas along the channel is influenced both by the electrostatic boundary conditions as well as charge distribution inside the transistor channel. Combining microscopic and macroscopic information with a simple mathematical model of the device, we are able to extract the electric field profile and charge carrier distribution (both static and dynamic) within the active organic material. In addition, exploiting the electron penetration depth lower than channel length, we develop an electro-optical technique for the measurement of AC mobility. We demonstrate that for phthalocyanine oTFT, AC mobility is insensitive to environmental-induced traps, which usually limit the continuous operations at room conditions.

Acknowledgments

J.C.-G. Acknowledges financial support from the Spanish Ministry of Science and Innovation through Programa Ramon y Cajal (RYC-2009-05475) and POLYDYE Project (TEC2010-21830-C02-02). The authors thank Dr. Mario Caironi for useful discussions.

References

[1] D. Braga, G. Horowitz, Adv. Mater. 21 (2009) 1–14.
[2] S.M. Sze, K.K. Ng, Physics of Semiconductor Devices, third ed., Wiley Interscience, 2007.
[3] N.C. Greenham, S.C. Moratti, D.D.C. Bradley, R.H. Friend, A.B. Holmes, Nature 365 (6447) (1993) 628–630.
[4] G. Yu, J. Gao, J.C. Hummelen, F. Wudl, A.J. Heeger, Science 270 (5243) (1995) 1789–1791.
[5] H. Sirringhaus, P.J. Brown, R.H. Friend, Nature 401 (6754) (1999) 685–688.
[6] S.R. Forrest, Nature 428 (6986) (2004) 911–918.
[7] H. Bassler, Phys. Status Solidi B 175 (1993) 15.
[8] V. Podzorov, E. Menard, J.A. Rogers, M.E. Gershenson, Phys. Rev. Lett. 95 (226) (2005) 601.
[9] J. Takeya, J. Kato, K. Hara, M. Yamagishi, R. Hirahara, K. Yamada, Y. Nakazawa, S. Ikehata, K. Tsukagoshi, Y. Aoyagi, T. Takenobu, Y. Iwasa, Phys. Rev. Lett. 98 (2007) 196804.
[10] P.G. Le Comber, W.E. Spear, Phys. Rev. Lett. 25 (1970) 509.
[11] M.C.J.M. Vissenberg, M. Matters, Phys. Rev. B 57 (12) (1998) 964.
[12] H. Vazquez, R. Oszwaldowski, P. Pou, J. Ortega, R. Perez, F. Flores, A. Kahn, Europhys. Lett. 65 (2004) 802.
[13] S. Braun, W.R. Salaneck, M. Fahlman, Adv. Mater. 21 (2009) 1450–1472.
[14] M. Caironi, C. Newman, R. Moore, D. Natali, H. Yan, A. Facchetti, H. Sirringhaus, Appl. Phys. Lett. 96 (2010) 183303.
[15] D.S.H. Charrier, M. Kemerink, B.E. Smalbrugge, T. de Vries, R.A.J. Janssen, ACS Nano 2 (2008) 622.
[16] C. Sciascia, N. Martino, T. Schuettfort, B. Watts, G. Grancini, M.R. Antognazza, M. Zavelani-Rossi, C.R. McNeill, M. Caironi, Adv. Mat. (2011), doi:10.1002/adma.201102410.
[17] T. Manaka, E. Lim, R. Tamura, M. Iwamoto, Nat. Photonics 1 (2007) 581–584.
[18] Z.Q. Li, G.M. Wang, N. Sai, D. Moses, M.C. Martin, M. Di Ventra, A.J. Heeger, D.N. Basov, Nano Lett. 2 (2006) 224–228.
[19] M. Celebrano, C. Sciascia, G. Cerullo, M. Zavelani-Rossi, G. Lanzani, J. Cabanillas-Gonzalez, Adv. Funct. Mater. 19 (2009) 1–6.
[20] J.H. Lee, C.C. Liao, P.J. Hu, Y. Chang, Synth. Met. 144 (2004) 279.
[21] J.D. Slinker, J.A. De Franco, M.J. Jaquith, W.R. Silveira, Y.-W. Zhong, J.M. Moran-Mirabal, H.G. Craighed, H.D. Abruna, J.A. Matohn, G.G. Malliaras, Nat. Mater. 6 (2007) 894–899.
[22] D. Natali, L. Fumagalli, M. Sampietro, J. Appl. Phys. 101 (2007) 014501.
[23] L. Li, Q. Tang, H. Li, W. Hu, J. Phys. Chem. B 112 (2008) 10405–10410.
[24] Z. Bao, A.J. Lovinger, J. Brown, J. Am. Chem. Soc. 120 (1998) 207.
[25] J. Cabanillas-Gonzalez, H.J. Egelhaaf, A. Brambilla, P. Sessi, L. Duò, M. Finazzi, F. Ciccacci, G. Lanzani, Nanotechnology 19 (2008) 424010.
[26] G. Weiser, Á. Horváth, Electro-absorption spectroscopy of π-conjugated polymers. Available from: <www.ipc.uni-linz.ac.at/publ/book/Chapter12.pdf> (Chapter 12).
[27] S.A. Whitelegg, Experimental Investigations into the Physics of Light Emitting Conjugated Polymers, Ph.D. thesis, Cambridge University (2001).
[28] P.J. Brown, H. Sirringhaus, M. Harrison, M. Shkunov, R.H. Friend, Phys. Rev. B 63 (2001) 125204.
[29] K. Yamasaki, O. Okada, K. Inami, K. Oka, M. Kotani, H. Yamada, J. Phys. Chem. B 101 (1997) 13–19.
[30] The applied electric field has two contributions: $\boldsymbol{F}_{Appl}(\mathbf{r}) = \boldsymbol{F}_{DC}(\mathbf{r}) + \boldsymbol{F}_{AC}(\mathbf{r})\cdot\sin(2\pi ft)$, consequently the ER signal will be: Signal $\sim \boldsymbol{F}_{App}{}^2(\mathbf{r}) = \boldsymbol{F}_{DC}{}^2(\mathbf{r}) + \mathbf{F}_{AC}{}^2(\mathbf{r}) + 0.5\cdot\boldsymbol{F}_{DC}(\mathbf{r})\cdot\boldsymbol{F}_{AC}(\mathbf{r})\cdot\sin(2\pi ft) - 0.5\,\boldsymbol{F}_{AC}{}^2(\mathrm{r})\cos(2\cdot 2\pi ft)$.
[31] M. Kitamura, T. Imada, S. Kako, Y. Arakawa, Jpn. J. Appl. Phys. 43 (2004) 2326.
[32] M. Caironi, Y.-Y. Noh, H. Sirringhaus, Semicond. Sci. Technol. 26 (2011) 034006.
[33] J.D. Jackson, Classical Electrodynamics, John Wiley & Sons, New York, 1975.
[34] N. Majumdar, S. Mukhopadhyay, v1 (2006).